The Three-Dimensional Structure and Kinematics of Drizzling Stratocumulus

KIMBERLY K. COMSTOCK AND SANDRA E. YUTER

Department of Marine, Earth, and Atmospheric Sciences, North Carolina State University, Raleigh, North Carolina

ROBERT WOOD AND CHRISTOPHER S. BRETHERTON

Department of Atmospheric Sciences, University of Washington, Seattle, Washington

(Manuscript received 6 July 2006, in final form 16 January 2007)

ABSTRACT

Drizzling marine stratocumulus are examined using observations from the 2001 East Pacific Investigation of Climate Stratocumulus (EPIC Sc) field experiment. This study uses a unique combination of satellite and shipborne Doppler radar data including both horizontal and vertical cross sections through drizzle cells. Stratocumulus cloud structure was classified as closed cellular, open cellular, or unclassifiable using infrared satellite images. Distributions of drizzle cell structure, size, and intensity are similar among the cloud-structure categories, though the open-cellular distributions are shifted toward higher values. Stronger and larger drizzle cells preferentially occur when the cloud field is broken (open-cellular and unclassifiable categories). Satellite observations of cloud structure may be useful to indicate the most likely distribution of rain rates associated with a set of scenes, but infrared data alone are not sufficient to develop routine precipitation retrievals for marine stratocumulus. Individual drizzle cells about 2–20 km across usually showed precipitation growth within the cloud layer and evaporation below, divergence near echo top, and convergence below cloud base. Diverging flow near the surface was also observed beneath heavily precipitating drizzle cells. As the cloud field transitioned from a closed to an open-cellular cloud structure, shipborne radar revealed prolific development of small drizzle cells (<10 km^2) that exceeded by over 5 times the number of total cells in either the preceding closed-cellular or following open-cellular periods. Peak area-average rain rates lagged by a few hours the peak in total number of drizzle cells. Based on observations from EPIC Sc, the highest stratocumulus rain rates are more likely to occur near the boundary between closed and open-cellular cloud structures.

1. Introduction

Low, warm stratocumulus clouds top the marine boundary layers in eastern subtropical oceans and exert a net radiative cooling effect on the climate (Hartmann et al. 1992). Because the simulated climatological structure of cloud-topped boundary layers is currently far from perfect in most atmospheric general circulation models, the radiative response of stratocumulus to changing climate conditions is a major source of uncertainty in climate simulations (Bony and Dufresne 2005; Bony et al. 2006; Cronin et al. 2006; Wyant et al. 2006). Cloud cover and optical thickness are the key parameters that must be predicted in these models in order to correctly represent low cloud radiative properties.

Viewed from above, stratocumulus clouds tend to form open or closed-cellular patterns. Closed-cellular stratocumulus show patterns of cloudy regions surrounded by thin clouds or clear air. Open-cellular stratocumulus, with clear regions surrounded by "rings" of clouds, can be found at the edge of, or within, closed-cellular stratocumulus sheets (see visible images in Fig. 1; Krueger and Fritz 1961; Atkinson and Zhang 1996; Stevens et al. 2005; Comstock et al. 2005; van Zanten et al. 2005; Sharon et al. 2006; Wood and Hartmann 2006).[1] Both types usually have aspect ratios of 30:1 to

Corresponding author address: Sandra Yuter, Dept. of Marine, Earth, and Atmospheric Sciences, North Carolina State University, Campus Box 8208, Raleigh, NC 27695.
E-mail: sandra_yuter@ncsu.edu

[1] Our use of the term "open cell" is not meant to imply that the microphysics and kinematics are necessarily the same in stratocumulus and open cells in midlatitude regions, for example, cold-air outbreaks.

DOI: 10.1175/2007MWR1944.1

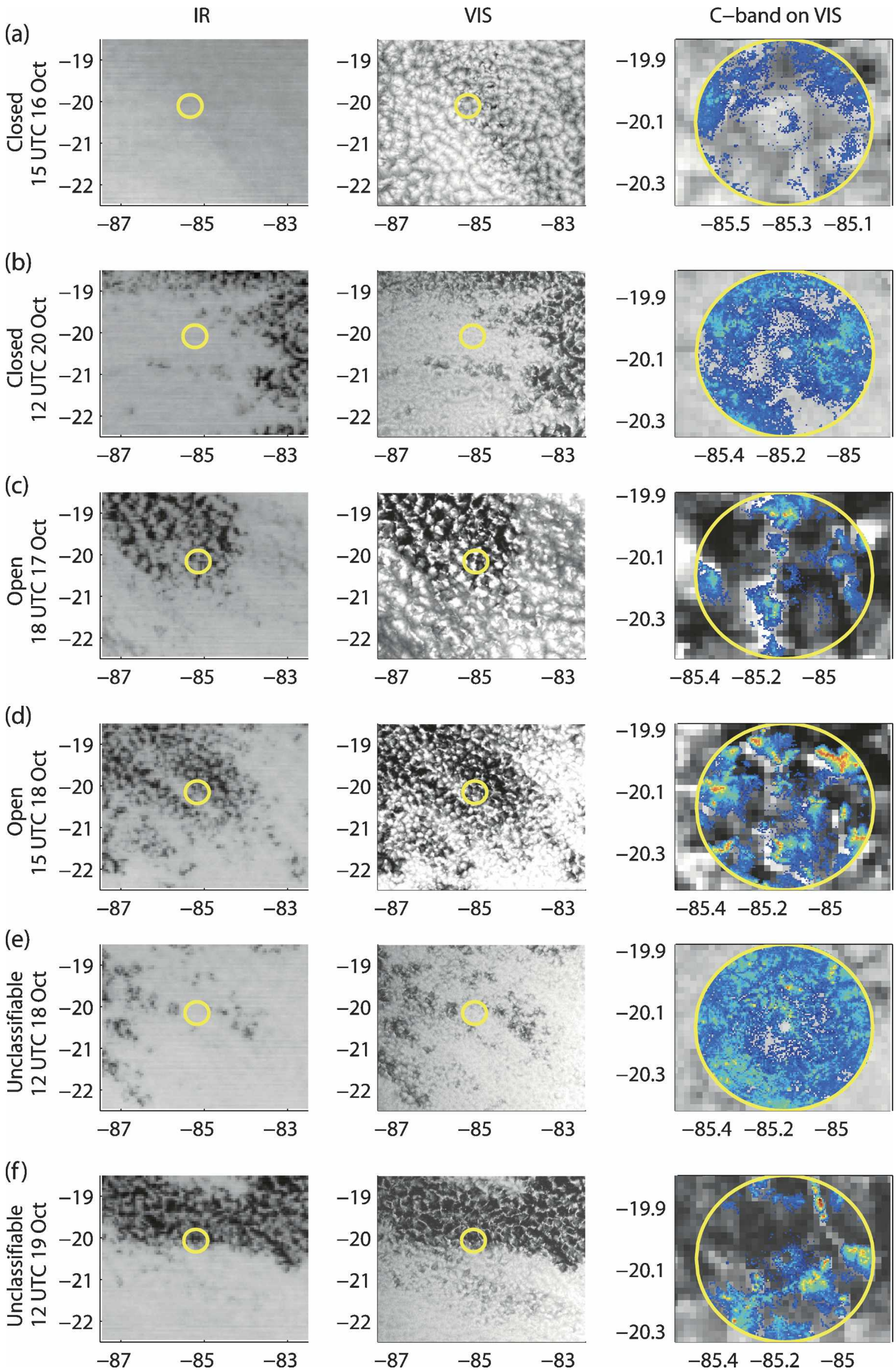

FIG. 1. GOES IR and VIS imagery and C-band radar reflectivity superimposed on the VIS image for two examples of each type of cloud structure: closed cellular at (a) 1500 UTC 16 Oct and (b) 1200 UTC 20 Oct 2001, open cellular at (c) 1800 UTC 17 Oct and (d) 1500 UTC 18 Oct 2001, and broken clouds in the unclassifiable category at (e) 1200 UTC 18 Oct and (f) 1200 UTC 19 Oct 2001. Yellow circles correspond to the 30-km-radius C-band data centered at the ship location. In IR images, lighter shades represent lower (colder) brightness temperatures, whereas in VIS images, lighter shades represent larger reflectance values. The ordinates and abscissa correspond to latitude (°N) and longitude (°E), respectively. The reflectivity color scale is the same as in Figs. 7–10.

40:1, but on average closed cells have a 30% higher cloud fraction (Wood and Hartmann 2006) and reflect significantly more solar radiation than open cells (Comstock 2006).

Precipitation may play a role in forming or maintaining the open-cellular structures. Recent studies found open-cellular regions contained higher rain rates compared with neighboring closed-cellular clouds (Stevens et al. 2005; Sharon et al. 2006). Van Zanten and Stevens (2005) explored the dynamics and thermodynamics of a region or "pocket" of open cells and presented a conceptual model showing the potential role of precipitation in breaking up the cloud layer (see also Paluch and Lenschow 1991; Feingold et al. 1996b; Stevens et al. 1998).

Improving parameterizations of stratocumulus will require a better understanding of the role of precipitation in modifying cloud structure, which, in turn, requires additional knowledge of the structure of precipitation within the various cloud patterns. In this study, we use observations from the 2001 East Pacific Investigation of Climate Stratocumulus study (EPIC Sc; Bretherton et al. 2004) obtained in the southeast Pacific to derive statistical information on precipitation within open- and closed-cellular stratocumulus. The unique EPIC Sc dataset includes high temporal and spatial resolution observations of clouds and drizzle from a scanning C-band radar. The radar provided both vertical and horizontal slices through an unprecedented number of stratocumulus drizzle cells over several days. The structure of radar-observed drizzle cells is also examined with respect to satellite-observed cloud patterns. The statistics documented here can be useful for comparison with future modeling studies.

The EPIC Sc data and instruments are described in section 2. Radar-observed characteristics of stratocumulus drizzle are characterized and related to the satellite-observed cloud-structure categories in section 3. Frequency distributions of rain rates suggest a complicated relationship between satellite-observed cloud structure and radar-derived precipitation amount. To develop a more detailed picture of the vertical structure of drizzle cells, images and statistics are derived from the C-band radar's previously unexploited range–height indicator (RHI) scans (section 4). A discussion of the transition between closed- and open-cellular types of cloud structures is presented in section 5, followed by concluding remarks in section 6.

2. Data sources and classification

All data used in this analysis are from the EPIC Sc "on-station period" (16–22 October 2001), while the National Oceanic and Atmospheric Administration (NOAA) Research Vessel *Ronald H. Brown* (*RHB*) was located in the heart of the southeast Pacific stratocumulus region at 20°S, 85°W (Bretherton et al. 2004).

The shipboard 5-cm-wavelength scanning C-band Doppler radar is sensitive to drizzle and heavier precipitation but not clouds (Ryan et al. 2002). The beamwidth was 0.95°. The C-band minimum-detectable reflectivity was about -12 dBZ at 30 km, and its calibration offset was estimated to be within ± 2.5 dBZ (Comstock et al. 2004). The scan strategy, described in appendix A of Comstock et al. (2004), included one 30-km-radius volume scan every 5 min and a set of four RHI scans (north, south, east, and west) 10 times an hour.

Volumetric C-band data were used in two ways. The 3D radial velocity (VR) and reflectivity (Z) data were vertically interpolated and area-averaged reflectivity statistics were derived. Vertical interpolation minimized the impact of C-band pointing-angle uncertainties (Comstock et al. 2004, appendix A). This is a reasonable method of inspecting the horizontal characteristics of the drizzle cells because the stratocumulus layer was quite thin (typically less than 500 m). Rain rates (R) were computed for each regridded reflectivity pixel using the reflectivity–rain-rate relationship derived in Comstock et al. (2004): $Z = 25R^{1.3}$. (Note that this relationship has a wide envelope of uncertainty, expressed in the bounding relationships $Z = 11R^{1.3}$ to $Z = 54R^{1.3}$.) Use of another Z–R relationship, such as the overall relationship in van Zanten et al. (2005), provides qualitatively similar results, though the magnitude of the rain rate is lower, particularly for reflectivity values above 3 dBZ. The 3D volume scans were also interpolated to resolutions of 250 m in the vertical and 500 m in the horizontal. This was used only for qualitative comparison of radial velocity within a small range of azimuth angles (e.g., $<45°$).

Detailed vertical cross sections were obtained using the C-band RHI scans. RHI reflectivity and radial velocity data were interpolated to resolutions of 75 m in the horizontal and 100 m in the vertical. Each scan was then normalized vertically with respect to the echo-top height. This was useful in circumventing differences in cloud-top height due to radar pointing-angle uncertainties as well as diurnal variations. An additional set of RHIs was computed for the purpose of determining a smooth radial divergence (RDIV) field. The 75-m-resolution RHIs were degraded to 500-m resolution using a 1–2–1 filter. Data below 200-m height and closer to the ship than 5 km were excluded from all RHI

TABLE 1. Data periods used for analysis in this paper during the EPIC Sc on-station period: 16–22 Oct 2001. All times are UTC. Subtract 6 h for local time.

Day	Closed-cellular structure	Open-cellular structure	Unclassifiable cloud structure
16	1230–1400, 1550–1700		
17	0820–0930	1730–1830	1130–1530, 2030–2130
18	0000–0930	1430–1920	1130–1230, 2330–2400
19		0230–0330, 0830–1230	0000–0030, 0530–0630, 1430–1645
20	0600–1230		1430–1530, 2330–2400
21	0300–0630	0830–0930, 1430–1830	0000–0030, 1130–1230

analyses to eliminate potential contamination from sea clutter.

Several figures in this paper show the anomalous radial velocity field, VR′. The latter was computed for each 3D scene by subtracting the radial velocity equivalent of a uniform wind field from the radar-observed VR field. The average VR at each azimuthal angle was calculated and the results were fit to a sine curve. The magnitude of the uniform wind field was estimated as the amplitude of the sine wave [similar to vertical azimuth display (VAD) analysis; Matejka and Srivastava (1991)]. For the RHIs, the mean value of VR was subtracted from all of the VR values in each cross section. A uniform wind field is a reasonable assumption in part because the soundings typically showed little wind shear in the boundary layer during EPIC Sc. In this paper, VR′ is used for display purposes only.

In addition to the C-band radar, the RHB was also equipped with a vertically pointing millimeter-wavelength cloud radar (MMCR; Moran et al. 1998). The MMCR data are used to estimate cloud-top height at the ship location. A shipboard laser ceilometer provided cloud-base heights. High temporal resolution surface meteorological measurements were also obtained aboard the ship (Comstock et al. 2005). Rawinsondes were launched every 3 h, and cloud photography was taken hourly during daylight.

NOAA Geostationary Operational Environmental Satellite (GOES) infrared (IR) imagery (10.2–11.2 μm) images were available every 3 h and were interpolated to 5-km resolution (Menzel and Purdom 1994). Reflectance, or effective albedo, was computed from the GOES visible (VIS) data at 0845, 1145, and 1445 local time (LT), accounting for calibration offsets, the solar zenith angle, and other geometrical factors (P. Minnis 2002, personal communication).

All GOES IR images were visually inspected for cloud structure within the radar domain observed from the ship. Those with clearly recognizable features were classified as having a closed-cellular (46% of images) or an open-cellular (26% of images) cloud structure. The remaining images were assigned to the "unclassifiable" category (28% of images), following the nomenclature used in Houze et al. (1990). The unclassifiable images have in common only that some broken clouds were present. This category also includes images when the ship appeared to be on the boundary between open and closed-cellular clouds. A more objective wavelet-based method failed to reliably identify cloud structure, particularly near cloud-sheet edges and other changes in cloud characteristics. The human eye can easily gauge relative differences that are difficult to distinguish with automated algorithms.

For this study, we selected a subset of drizzling cloud radar data with detectable C-band echo. This set includes approximately 16 h of open-cellular and 23 h of closed-cellular drizzling cloud data as well as 14 h of data in the unclassifiable category. Specific time periods for each category are listed in Table 1.

3. Precipitation and cloud structure

a. Rain-rate distribution

Precipitation falling in the form of drizzle from stratocumulus clouds is often reported to be patchy and intermittent (e.g., Nicholls 1984; Austin et al. 1995; Yuter et al. 2000; Stevens et al. 2003; Wood 2005; van Zanten et al. 2005). The C-band radar data from EPIC Sc can be used for both qualitative and quantitative assessments of this variability. Figure 1 shows daytime examples of precipitation in each of the three cloud-structure categories. Satellite IR and VIS images provide context for the radar data. The closed-cellular cloud structures are associated with patchy light drizzle conditions (Figs. 1a and 1b). If there is an overall structure to the drizzle, it may be on a scale too large to be observed within the 30-km-radius radar field of view. When the cloud structure is open cellular, the precipitation is more distinctly organized (clumpy) and also has greater variability in intensity (Figs. 1c and 1d).

The unclassifiable category includes periods when the cloud sheet is broken but does not clearly exhibit solely open- or closed-cellular structures. Figure 1e de-

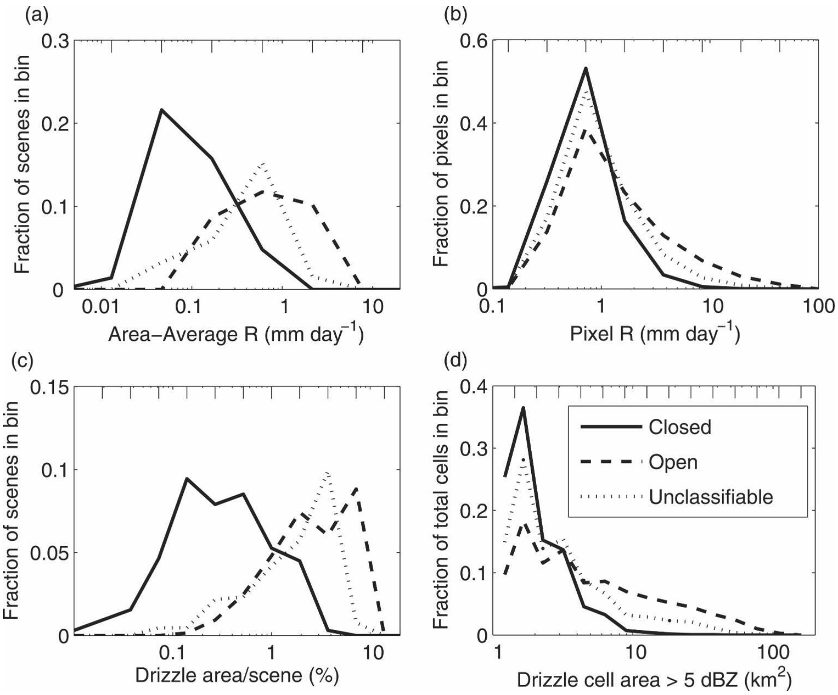

FIG. 2. (a) PDF of area-averaged cloud-base rain rate for closed-cellular, open-cellular, and unclassifiable cloud structures. (b) PDF of pixel rain rates (500 m $\times$ 500 m pixels in interpolated 2D radar data) over all scenes in each cloud-structure category. (c) PDF of drizzling area fraction (in %) for each cloud-structure category, i.e., pixel area for reflectivity $\geq$5 dBZ. (d) PDF of individual drizzle cell areas for all scenes with closed-cellular (solid), open-cellular (dashed), and unclassifiable cloud structures (dash–dot). Drizzle cells are defined as contiguous regions of $Z \geq 5$ dBZ. Bin edges are marked at the top of each plot.

picts an early morning scene (1145 UTC or 0545 LT) when a closed-cellular cloud sheet was beginning to break up. At the time of the image, the radar echo is still relatively unstructured, but small cellular echo regions are beginning to appear. Figure 1f illustrates an unclassifiable scene where the ship is on the boundary between closed- and open-cellular clouds.

Closed-cellular cloud structure tends to be associated with lower area-average cloud-base rain rates (peak rain rates <1.2 mm day^{-1}), while the rain-rate distributions for broken clouds (open-cellular and unclassifiable categories) are shifted toward higher rain rates, including several high values (>2 mm day^{-1}; Fig. 2a). In considering individual pixel rain rates (rain rate for each 500 m $\times$ 500 m pixel in the interpolated 2D radar data) over all scenes in each cloud structure category, broken clouds are associated with a slightly wider distribution of rain rates, containing a greater number of instances of high rain rates than closed-cellular clouds (Fig. 2b). While there is a tendency for lower area-average rain rates to be more common in closed-cellular regions compared to open-cellular regions, the latter can also exhibit low rain rates. For individual satellite scenes, information on cloud structure alone is insufficient to estimate area-average rain rate, rainy area, or drizzle cell size.

Throughout this analysis, "drizzle cells" are defined as contiguous regions with $Z \geq 5$ dBZ, equivalent to an instantaneous cloud-base rain rate of about 5 mm day^{-1} over a 500 m $\times$ 500 m pixel (Comstock et al. 2004). More than one drizzle cell may appear within the cloudy regions of stratocumulus open and closed cells. Scenes with broken clouds tend to have a greater area containing drizzle (Fig. 2c) compared with closed-cellular scenes. This result is qualitatively similar regardless of the dBZ threshold chosen.

Drizzle cells tend to be small in scenes with closed-cellular stratocumulus (<10 km^2) and can reach much larger sizes in scenes with broken clouds (open cellular and unclassifiable, e.g.; Fig. 2d). For scenes where drizzle cells are contiguous and indistinct (such as in closed-cellular category and some scenes in the unclassifiable category; Figs. 1a, 1b, and 1e), the precise distribution of drizzle cell areas is somewhat dependent on the reflectivity threshold chosen. This is less true of open-cellular periods where drizzle cells tend to be

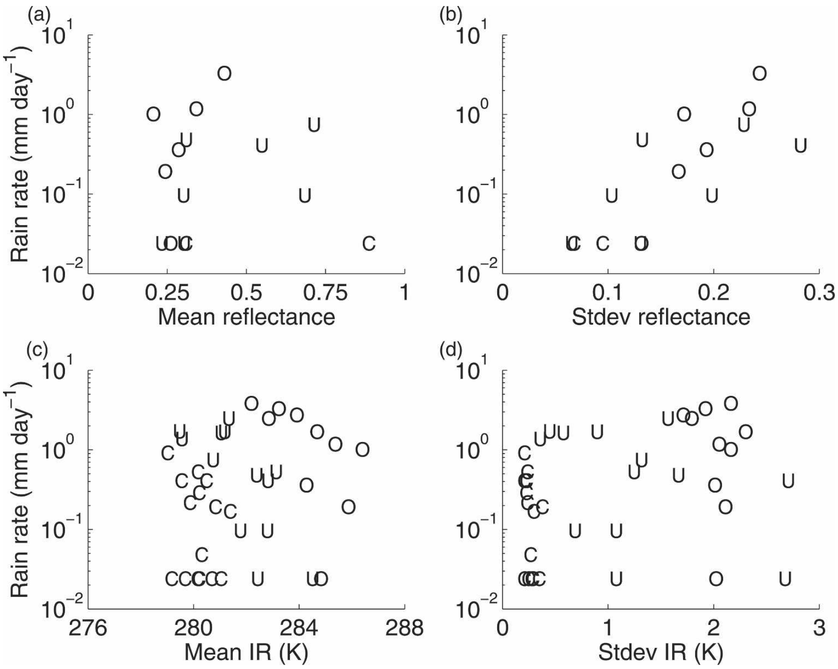

FIG. 3. Area-averaged cloud-base rain rate vs (a) mean reflectance and (b) standard deviation of reflectance from GOES VIS images during the day. Reflectance is on a scale of 0 to 1. (c) Mean IR brightness temperature and (d) standard deviation of IR brightness temperature. Letters indicate closed-cellular (C), open-cellular (O), and unclassifiable (U) cloud structures. All values are computed within a 30-km radius of the ship. The only statistically significant correlation is in (b) with a squared correlation coefficient of 0.6.

more isolated, separated by nondrizzling clouds or clear air (Figs. 1c and 1d).

b. Relationship of satellite and radar-derived properties

In section 3a, we saw that knowledge of cloud structure indicates the distribution of likely rain rates, although it is insufficient to predict the area-average rain rate of a scene. Satellite IR and VIS observations are more readily available than precipitation retrievals. In this section, we explore the extent to which simple satellite-observed cloud characteristics are correlated with radar-derived precipitation amount. The results are mixed. As expected for broken clouds, open-cellular scenes have lower-mean daytime reflectance (Fig. 3a) and higher-mean IR brightness temperature (Fig. 3c). Daytime scenes with greater variability (open and unclassifiable categories) tend to correspond to higher area-average rain rates (Fig. 3b). This suggests that for daytime scenes, high rain rates and more variable visible reflectance are both associated with high variability in liquid water path (Stevens et al. 1998). Using standard deviation of IR brightness temperature for scenes throughout the day and night did not yield a similar pattern. Figure 3d shows that clouds can be broken without precipitation. Clearly, cloud variability is only one factor tied in with precipitation production.

Another factor to consider is the diurnal cycle, long known to be important in modulating stratocumulus cloud thickness and therefore cloud fraction (e.g., Turton and Nicholls 1987; Minnis et al. 1992; Rozendaal et al. 1995) and stratocumulus production of drizzle. During EPIC Sc, drizzle fell throughout the day, but mostly in the early morning (Comstock et al. 2005). In the afternoon, clouds can be variable (in the IR) without high rain rates, but high cloud-top temperature variability in the early morning or nighttime is usually associated with higher rain rates (Fig. 4).

c. Relationship of cloud structure to boundary layer properties

In previous work, observations from EPIC Sc were divided into periods where the boundary layer was well mixed (coupled), periods where it was not well mixed ("less coupled"), and those when there was drizzle in the vicinity of the ship (Comstock et al. 2005). The criteria for drizzle was met when the area of reflectivity greater than 5 dBZ was larger than about 4% of the

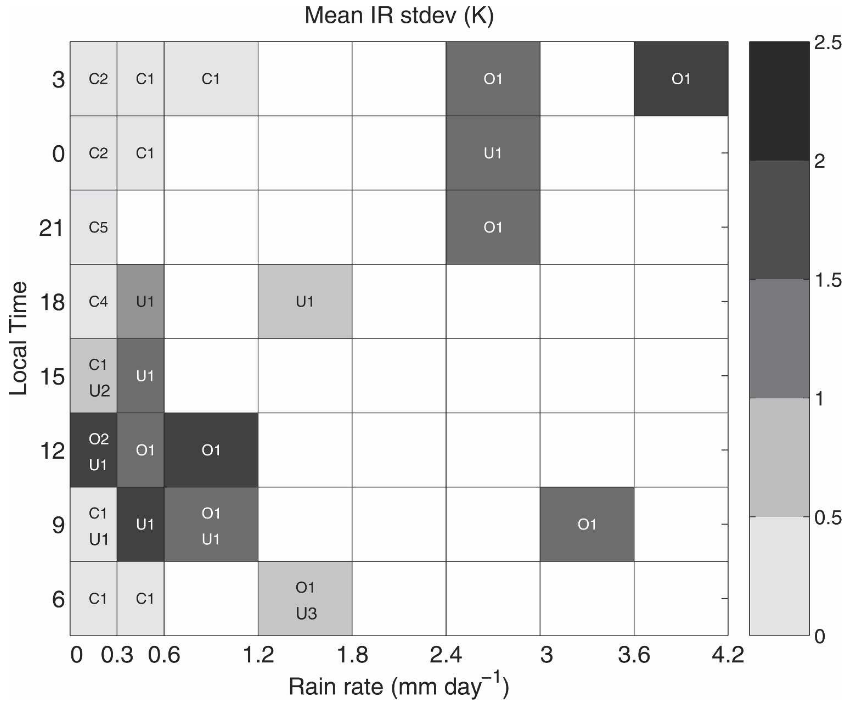

FIG. 4. Mean GOES IR standard deviation (gray shaded) sorted by area-average cloud-base rain rate and local time of day. The number of samples in each cloud structure category (C, closed cellular; O, open cellular; U, unclassifiable) is indicated by the number(s) in each box.

C-band echo area. Nondrizzling periods were classified as coupled when the difference between hourly cloud-base height and lifting condensation level (computed from surface values of temperature and moisture) was less than 300 m. Otherwise, the boundary layer was considered less coupled.

Figure 5 (see also Table 2) illustrates how these thermodynamic categories fit with the cloud-structure cat-

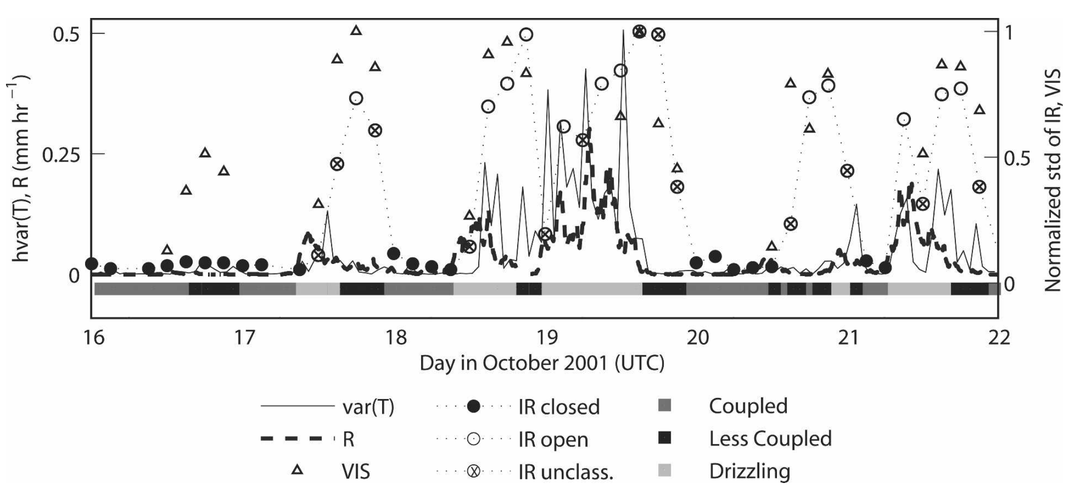

FIG. 5. Time series of hourly averaged variance of surface air temperature, hvar(T) (solid), and hourly area-averaged cloud-base rain rate (dashed) on the left ordinate, and on the right ordinate, mean IR brightness temperature T_b (dotted, circles) and mean VIS reflectance (triangles) within a 30-km radius of the ship. Standard deviations of IR and VIS are normalized to a maximum value of 1. Filled circles indicate closed-cellular cloud structure, open circles indicate open-cellular cloud structure, and circles with x's inside indicate unclassifiable cloud structure. The gray scale at the bottom of the figure indicates coupled (medium gray), less-coupled (black), and drizzling (light gray) periods.

TABLE 2. Tabular form of time series in Fig. 5. For each cloud-structure category (closed, open, and unclassifiable), the number of satellite images is shown, as well as the number of images coinciding with each thermodynamic category (coupled, less coupled, and drizzling). The final column shows the total number of C-band radar scenes in each cloud-structure category. One open-cellular satellite image could not be classified due to missing data.

Cloud structure	Total no. of images	Coupled	Less coupled	Drizzling	C-band scenes
Closed	21	18	2	1	721
Open	12	1	4	6	264
Unclassifiable	13	0	7	6	228

egorization scheme discussed in this paper. Most of the closed-cellular periods occurred while the boundary layer was well mixed (coupled). Occasionally, the clouds thinned but remained closed cellular after the boundary layer became less well mixed in the afternoon (e.g., 16 October in Fig. 5). Both the coupled and closed-cellular categories have relatively homogeneous cloud and boundary layer properties with little precipitation and low variability in surface temperature, T, and IR brightness temperature. These conditions describe typical stratocumulus, where cloud-top radiative cooling drives circulations that keep the boundary layer well mixed.

Open-cellular cloud structure was associated with drizzling and less-coupled periods (Table 2). Variability in surface air temperature was particularly high during open-cellular periods (Fig. 5). This variability is caused in part by evaporative cooling from intermittent precipitation and in part because the boundary layer is not well mixed (Paluch and Lenschow 1991; Stevens et al. 1998; Comstock et al. 2005).

Variability in air–sea temperature difference is highly correlated with variability in surface air temperature because the sea surface temperature varies relatively slowly. The air–sea temperature difference for open cells that appear in cold-air outbreaks (mentioned in the introduction) is typically between 2° and 5°C (Atkinson and Zhang 1996). The mean air–sea temperature difference in open-cellular periods during EPIC Sc was about 2.3° ± 0.5°C, 1°C larger than for the closed-cell periods. The increased air–sea temperature difference during precipitation may be important in maintaining the open-cellular structure in stratocumulus (e.g., Jensen et al. 2000) by enhancing the surface buoyancy of convection, allowing convective updrafts to become more vigorous and cumuliform when they reach the lifting condensation level. During the EPIC Sc on-station period, larger air–sea temperature differences were associated with greater sensible heat fluxes (squared correlation coefficient = 0.6), but not with increased latent heat fluxes.

Changes in boundary layer wind speed do not appear to be related to the appearance of open-cellular cloud structure. For example, the increased wind speeds on 19 and 20 October (Fig. 6) do not correspond to increased or prolonged periods of open-cellular cloud structure (Fig. 5). During EPIC Sc, trade winds consistently blew from the southeast and east-southeast. Because there is no preferred shear structure in speed or direction that corresponds with changes in cloud structure in the southeast Pacific boundary layer, shear is unlikely to be a factor in determining cloud organization.

4. Vertical cross sections of drizzle cells

a. Examples

In this section, the vertical structures of drizzle cells within each cloud-structure category are examined. We have chosen three examples to illustrate the drizzle cells' kinematic structure. The first example occurred under unbroken, closed-cellular clouds. Figures 7a and 7b show slices of reflectivity and anomalous radial velocity through the 3D C-band volume scans. The 270° RHI extends 30 km westward from the ship and bisects several small drizzle cells. Cross sections of Z, VR′, and the radial component of the divergence, derived from this RHI, are shown in Figs. 7c and 7e.

Examining the drizzle cell between 8 and 12 km away from the ship, the VR′ profile shows horizontal flow into the cell below about 1-km altitude and horizontal outflow above 1 km (Fig. 7d). The computed radial divergence signal peaks near cloud top between about 10 and 12 km from the ship where reflectivity is strongest (Fig. 7e). Convergence in this cell is observed over a deeper layer than the divergence (about 300–900-m versus 1–1.3-km altitude); inflow and outflow in the radial direction appear to be roughly balanced in this cell. The echo-top outflow structure observed in the 270° RHI is also evident in the plan view of VR′ (Fig. 7b). Figure 7f shows the completely overcast sky associated with the early morning closed-cellular stratocumulus. Leon (2006) found similar structures in unbroken stratocumulus using observations from vertically pointing as opposed to scanning radar. In that study, observed drizzle cells were small (usually 3–5 km in horizontal scale), which is consistent with our findings for closed-cellular periods (Fig. 2d). Leon (2006) noted that the overturning kinematic structures of drizzle cells were embedded within larger, mesoscale circulations.

An example during an open-cellular period is shown in Fig. 8. The 90° RHI bisects one strong drizzle cell

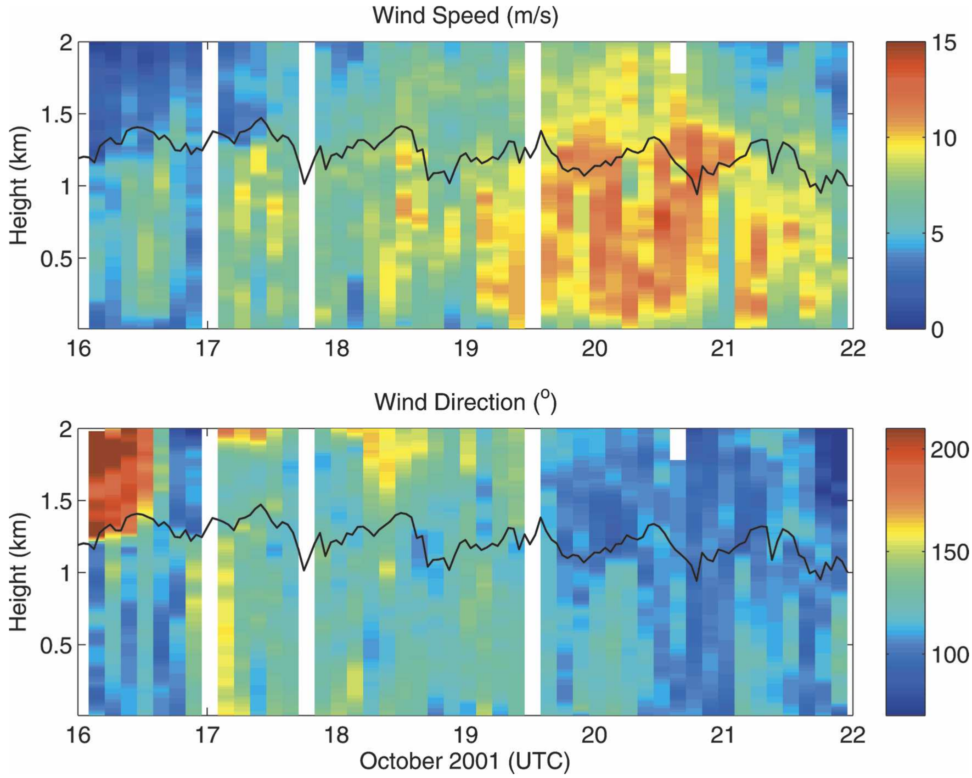

FIG. 6. Time–height cross sections of wind speed and direction from 3-hourly radiosondes during the EPIC Sc field campaign. Solid black line shows hourly cloud-top height from the MMCR.

between about 14 and 18 km away from the ship. Again, the radial convergence is observed in a deeper layer (up to about 700 m) than the radial divergence (about 900 m–1.2 km), and the latter is stronger by about 1 m s^{-1} km^{-1} at the top of the cell (Fig. 8e). For this drizzle cell, flow diverges near the echo top. Divergence extends over the 20-km length of the drizzle cell in the upper-right quadrant of Fig. 8f. There is a break in the clouds near some of the strong drizzle cells in this scene (Fig. 8f).

The final example is one that occurred as the cloud field was transitioning from an open- to a closed-cellular cloud structure. The drizzling portion of the cloud feature, as captured by a composite of cloud photographs (Fig. 9f), is about 30 km in length and up to 12 km wide. The stratocumulus cloud thins at the edges and is surrounded by regions of patchy cloud and clear sky (Fig. 9f). The drizzle cell bisected in Fig. 9 displays the typical subcloud inflow and cloud-level outflow pattern described previously. The outflow pattern observed in the RHIs continues along the entire length of the drizzle cell (Fig. 9b).

Convergence below strongly drizzling cells has been shown to be common. Divergence near the sea surface was also observed in a few RHIs where the radar signal was not obscured by sea clutter (10 examples). The observed radial outflow near the surface in Fig. 10 was most likely associated with a cold pool formed by the evaporation of drizzle. Similar to microbursts in convective storms (Kingsmill and Wakimoto 1991), such outflow is likely the result of evaporatively cooled downdrafts and can contribute to surface convergence that may strengthen nearby updrafts (Jensen et al. 2000; see also conceptual models in Fig. 12b of Comstock et al. 2005 and Fig. 10 of van Zanten and Stevens 2005).

b. Statistical representations of vertical cross sections

The properties of drizzling stratocumulus are now summarized using statistics computed over all vertical cross sections (RHI scans) and over all the drizzle cells identified in each cloud-structure category. In this portion of the analysis, we only include drizzle cell cross sections with a vertically and horizontally continuous region of $Z \geq 5$ dBZ of at least 750 m in height and width. The mask corresponding to each drizzle cell includes all heights ($z \geq 200$m) for the entire width of the drizzle cell ($x_c - 0.5w \leq x \leq x_c + 0.5w$), where x_c is the center and w is the maximum width of the cell at any height. Example drizzle cells are outlined by boxes in

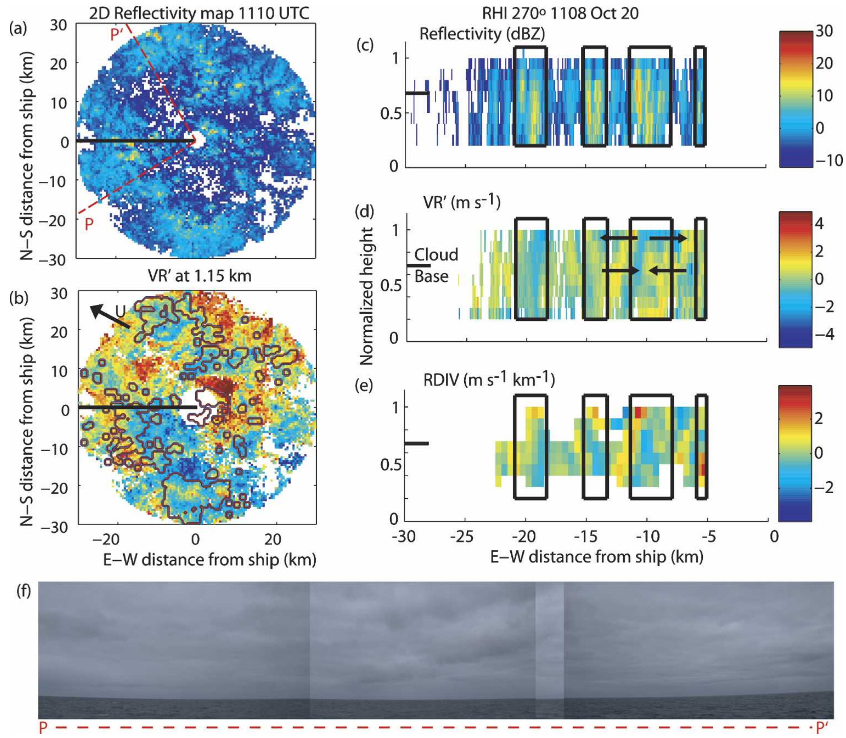

FIG. 7. Closed-cellular example. (a) A 2D reflectivity map at 1110 UTC 20 Oct 2001. Reflectivity averaged between 1.15- and 1.4-km height. Solid line indicates position of 270° RHI. (b) Anomalous radial velocity (VR′) from 3D C-band data at 1110 UTC at 1.15-km height. Flow away from the radar is positive; toward the radar is negative. The 5-dBZ contours (at 0.6-km height) are drawn to highlight the location of the drizzle cells. The 270° RHIs at 1108 UTC showing (c) reflectivity, (d) VR′, and (e) radial divergence. Color bars for reflectivity and VR′ also correspond to (a) and (b), respectively. Cloud-base height is indicated in each RHI. The hourly cloud base from the shipboard ceilometer is indicated in each of the cross sections, and boxes outline the identified drizzle cells (see section 4b). Arrows (not drawn to scale) indicate regions of inflow and outflow. (f) Composite cloud photo taken aboard the ship at 1115 UTC, looking from the southwest (P) to the northwest (P′). The projection of P–P′ is shown with dashed lines in (a).

Figs. 7 and 8. The all-Z category includes the entire RHI for each cloud-structure type, neglecting only $x < 5$ km and $z \leq 200$ m to minimize the effects of sea clutter.

Each subset of data was analyzed separately by creating contoured frequency–altitude diagrams (CFADs). A CFAD is a joint frequency distribution at each altitude (Yuter and Houze 1995). To compute the CFADs, histograms of Z and RDIV were calculated at each height and then normalized by the total number of data points at that height. To avoid biasing the results by using too few samples, data at a given height were excluded if the ratio of the number of samples at that height to the maximum number of samples at any height was less than 0.2.

The all-Z CFAD shows a wide range of reflectivity values throughout the boundary layer (Fig. 11a). In each cloud-structure category, drizzle cell reflectivity tends to increase with decreasing height below cloud top, indicating precipitation particle growth from the top of the cloud to cloud base. Decreasing Z below cloud base (about $0.6z_{\text{top}}$) is evidence of below-cloud evaporation. Rain rate will decrease more rapidly than reflectivity below cloud base because the large droplets that contribute most to the reflectivity will evaporate more slowly than the small droplets that contribute most to the rain rate in drizzling stratocumulus (see also Wood 2005). The reflectivity structure also qualitatively resembles ensemble characteristics for weak drizzle cells in a shallower boundary layer in the northeast Pacific (Vali et al. 1998). Drizzle cells exhibit somewhat lower peak reflectivity magnitudes and stronger signatures of below-cloud evaporation during closed-cellular periods than during open-cellular periods. The open-cellular periods are more heterogeneous and correspond to the widest distribution of reflectivity values at any given altitude.

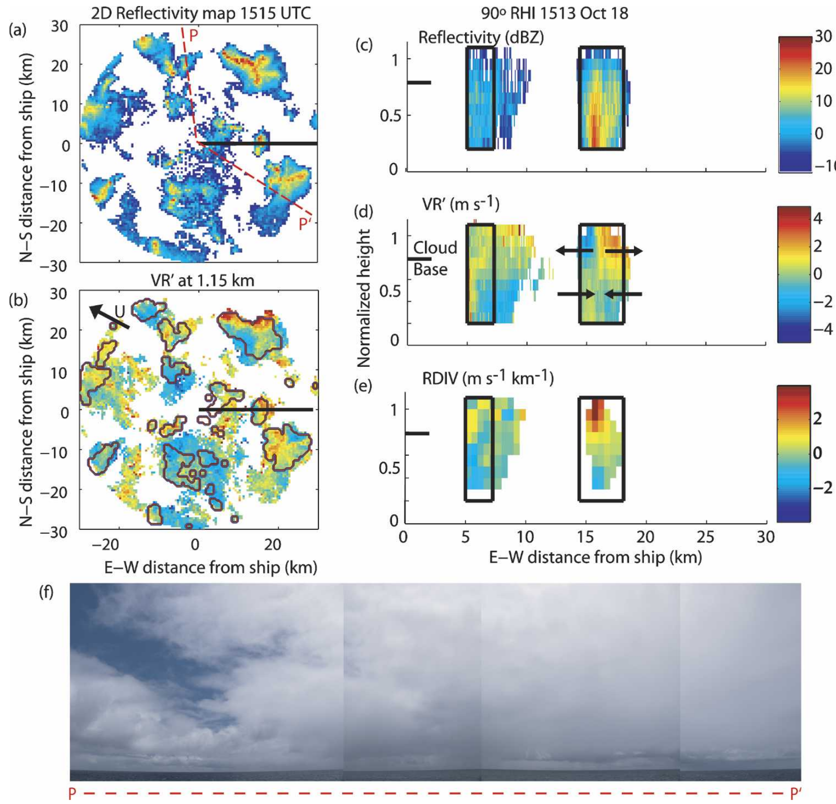

FIG. 8. Open-cellular example. (a)–(e) As in Fig 7 but for 90° RHI at 1515 UTC 18 Oct. (f) Composite cloud photo taken aboard the ship at 1515 UTC, looking from the north (P) to the southeast (P′). The projection of P–P′ is shown with dashed lines in (a).

Although drizzle cells contain a broad range of convergence and divergence strengths on the ~1 km scale (Figs. 7–9), they are characterized by a slightly greater frequency of convergence than divergence, as shown in the CFAD in Fig. 12a. Examining only the drizzle cell cores isolates the convergence and divergence where up-/downdrafts are likely to be strongest. Drizzle cell cores, defined here as columns that contain $Z \geq 10$ dBZ, show somewhat greater tendencies for convergence at low to midlevels (0.2–$0.6z_{\mathrm{top}}$) and divergence within the cloud layer ($>0.8z_{\mathrm{top}}$; Fig. 12). Drizzle cell cores with higher reflectivity tend to have slightly larger midlevel convergence and echo-top divergence signatures (not shown). Some of the overall spread in the CFADs may be due to noise in the data, but we expect this to be a random signal at all levels that would not contribute to the observed trend with height. Overall, the kinematic structure of the drizzle cell cores in all cloud-structure categories is similar. In the EPIC Sc dataset, strong drizzle cell cores were more often observed in conjunction with broken clouds (open-cellular or unclassifiable scenes) rather than closed-cellular periods (Table 3), despite the greater number of observations during closed-cellular conditions (Table 1).

Assuming that the convergence below cloud is isotropic (and thus RDIV only represents half of the actual convergence), implied vertical velocities can be estimated from mass continuity.[2] The modes of the RDIV CFADs in Fig. 12 imply frequent weak updrafts in drizzle cell cores, about 0.5–0.75 m s^{-1} from 200 to 800 m height over 500 m × 500 m horizontal pixels. The combination of filtering the radial velocity field and computing statistics over a large number of drizzle cells (>1000 drizzle cells with >350 drizzle cell core columns) contribute to the smoothness of the CFAD features. The frequency contours in Fig. 12 encompass implied vertical velocities of −1.4 to 2.2 m s^{-1}.

The divergence distributions are not vertically symmetric. That is, in the drizzle cell cores there appears to be a greater depth of convergence below cloud than divergence in the cloud layer where a radar echo is present. This suggests that to maintain mass balance, there is strong outflow in nonprecipitating regions

[2] The large number of RHIs in four directions through randomly oriented drizzle cells justifies the assumption that the results are not biased by the restriction of the data to the radial direction.

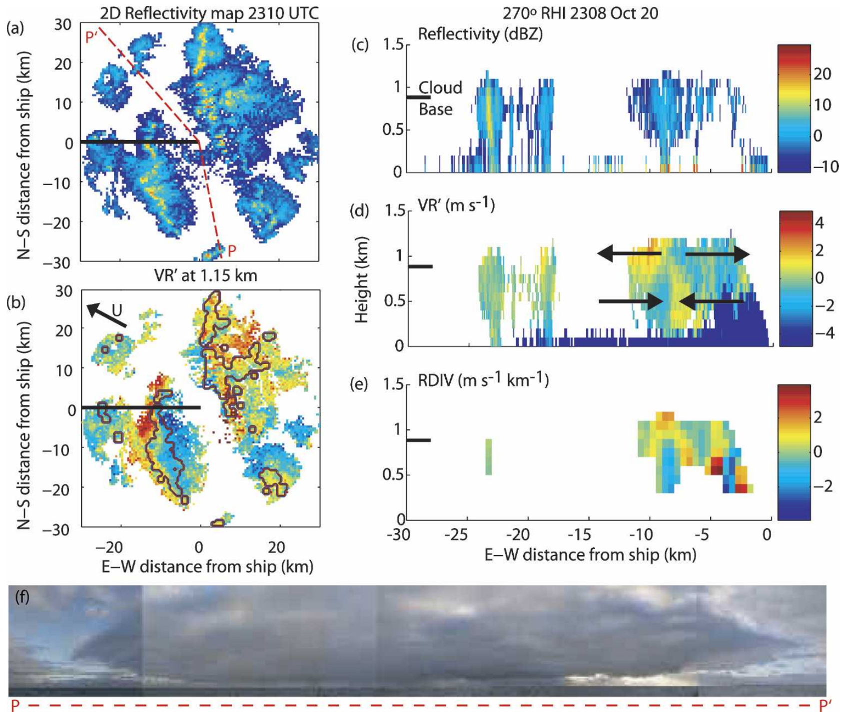

FIG. 9. Example from the unclassifiable cloud-structure category. In this case, cloud structure is transitioning from open to closed cellular. (a)–(e) As in Fig. 7 but for 2310 UTC and 270° RHIs at 2308 UTC 20 Oct. (f) Composite cloud photo taken aboard the ship at 2315 UTC, looking from the south-southeast (P) to the northwest (P′). The projection of P–P′ is shown with dashed lines in (a).

where velocity is not detected by the C-band radar, near the top of the cloud or outside of the drizzle cell cores. See conceptual model figures in Comstock et al. (2005; Fig. 12b) and van Zanten and Stevens (2005; Fig. 10).

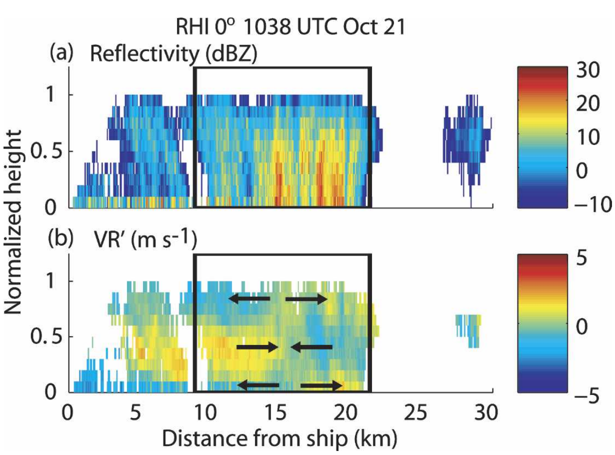

FIG. 10. Example of near-surface divergence in a drizzle cell transected by the 0° RHI at 1038 UTC 21 Oct (open-cellular cloud structure): (a) reflectivity and (b) anomalous radial velocity, VR′, where negative velocity is toward the radar. Arrows represent directions of radial inflow and outflow and are not drawn to scale.

Precipitating cells in stratocumulus appear to be scaled-down versions of their deep-convective cousins. Compared to tropical open-ocean cumulus convective cells, stratocumulus drizzle cells are weaker and shallower, and precipitation is more likely to evaporate completely before reaching the surface [cf. Fig. 11c with reflectivity CFADs shown in Yuter et al. (2005)]. However, the distribution of convergence magnitudes is similar to that within deep convective regions [cf. Fig. 12a with divergence CFADs in Yuter et al. (2005)]. Drizzling stratocumulus encompass the liquid phase precipitation processes that occur in deep convection including condensation, accretion, and advection (fallout) but not including ice and melting-layer processes.

5. Transition from closed to open-cellular cloud structure

Open-cellular areas frequently appear in otherwise closed-cellular stratocumulus sheets. Figure 13 illustrates the transition from a closed- to an open-cellular cloud structure where the breakup of the clouds appears to be coincident with the formation of strong, distinct drizzle cells. In this example, the cloud sheet

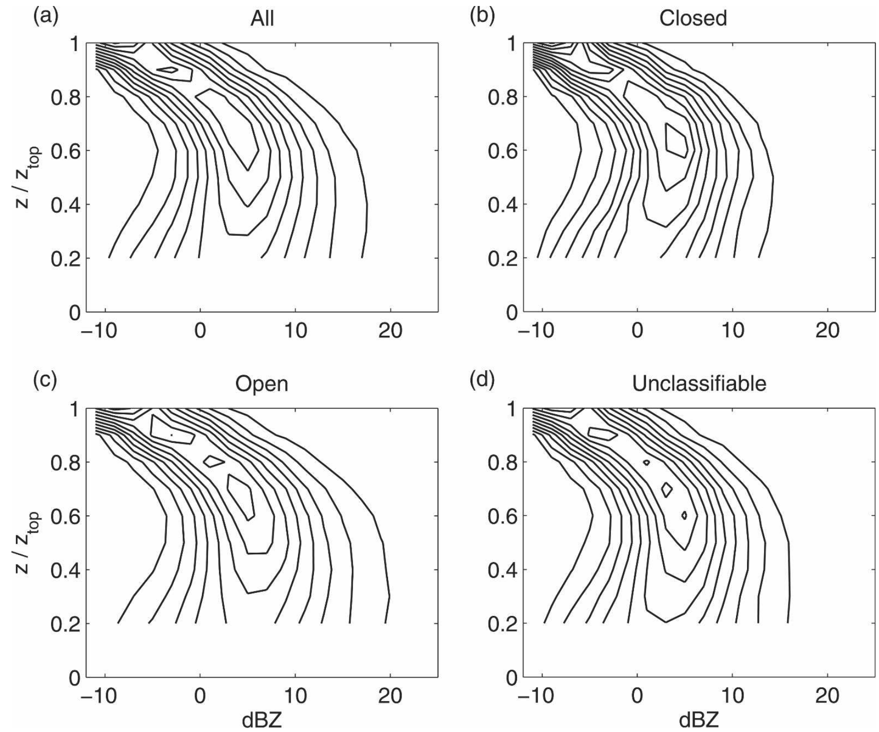

FIG. 11. CFADs of reflectivity for (a) all reflectivity and for the ensemble of drizzle cells in scenes with (b) closed-cellular, (c) open-cellular, and (d) unclassifiable cloud structures. Bin size is 2 dBZ, height increment is 100 m, and contour interval is 2%. The ordinate is height normalized to cloud top.

was characterized by closed-cellular structure for several hours prior to 0900 UTC (0300 LT) on 18 October 2001. At 0900 UTC, the scene was completely overcast with closed-cellular cloud structure (Fig. 13a). There are several regions with too little precipitation to be detected by the C-band radar (Fig. 13d). The area-averaged cloud-base rain rate for this scene is 0.4 mm day^{-1} (Fig. 14b). At 1200 UTC, the cloud sheet was broken and the cloud structure was not clearly open or closed cellular (unclassifiable category). The cloud field structure was clearly open cellular at 1500 UTC and for several hours thereafter. Between 1400 and 1500 UTC, the drizzle became more cellular and more intense. Breaks appeared in the radar images between the drizzle cells (Figs. 13f and 13g). In the 1500 UTC radar image, several distinct drizzle cells are clearly visible. During the transition, the drizzle intensity increased considerably, from 1.7 mm day^{-1} at 1200 UTC to a high of 3.3 mm day^{-1} at 1500 UTC (Fig. 14b).

Between 0000 and 0900 UTC, the closed-cellular stratocumulus contained only a few drizzle cells, or regions of reflectivity ≥5 dBZ. These cells were all small in size (area <10 km^2; Fig. 14a). The number of smaller drizzle cells increased by more than a factor of 5 between 0900 and 1200 UTC. The increase in the number of larger cells slightly lagged this prolific production of smaller cells. After 1500 UTC, the total number of drizzle cells fell. The decrease in the number of smaller cells was followed by a reduction in the number of larger cells until finally the open-cellular cloud sheet was supporting only a few large and small drizzle cells.

The prevailing wind in the southeast Pacific stratocumulus region is southeasterly, and the small open-cellular regions within the cloud sheet [so-called pockets of open cells or POCs; Stevens et al. (2005)] tend to advect roughly with the mean wind. Interestingly, in Figs. 13a and 13c, the open-cellular cloud structure appears to be growing against the mean wind by incorporating new POCs toward the southeast.

The effects of the diurnal cycle cannot be disentangled from the transition depicted in Figs. 13 and 14. The cloud layer may be more likely to thin or break up after sunrise (around 1200 UTC). However, open-cellular regions often appear before sunrise, so solar radiation alone is not sufficient to break up the cloud layer into an open-cellular structure (Comstock 2006).

The production of drizzle also tends to increase in the predawn hours as the clouds thicken. This may have an effect on the proliferation of drizzle cells in the early morning within regions of cloud-structure transition.

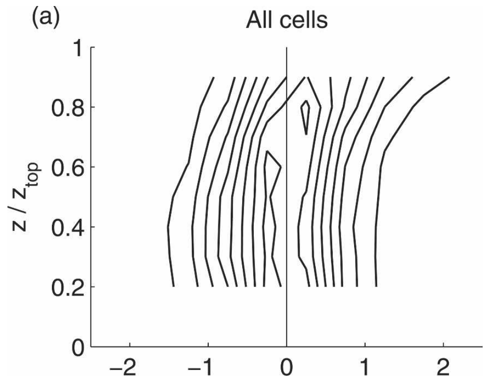

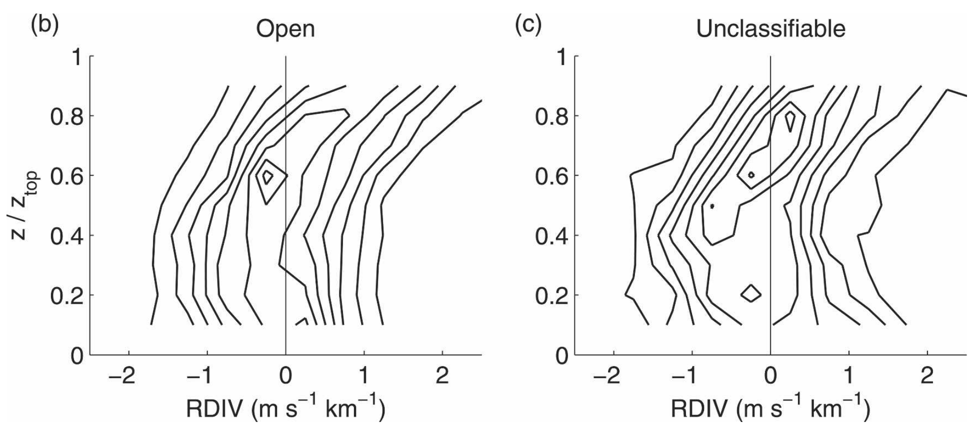

FIG. 12. CFADs of radial divergence for (a) all RHIs and for the ensemble of drizzle cell cores in the (b) open-cellular and (c) unclassifiable cloud-structure categories. There were too few data points in strong drizzle cell cores in the closed-cellular category to obtain robust statistics, so that category is not included here. The bin size is 0.25 m s^{-1} km^{-1}, height increment is 100 m, and contour interval is 4%. The ordinate is height normalized to cloud top. The mean profiles of RDIV are significantly different from zero, using 95% confidence intervals (not shown) that are 1×10^{-4} to 4×10^{-4} m s^{-1} km^{-1}.

However, a second transition example was examined during the afternoon with similar results to those presented in Figs. 13 and 14. Throughout the on-station period of EPIC Sc, rain rates tended to increase near the edges of open-cellular regions (Fig. 15). Consistent with findings documented elsewhere in this paper, there is a broad distribution of rain rates within and on the edge of open cellular regions, while observations obtained within cloudy regions far from open-cellular edges are skewed toward low rain rates.

In the example presented here, greater area-average rain rates are associated both with the increase in the overall number of drizzle cells produced and with the presence of a few large drizzle cells (Fig. 14). Stronger updrafts are necessary to create higher rain rates and reflectivity values. In this example, the area of high reflectivity (>5 dB*Z*) increases simultaneously with the transition from a closed- to an open-cellular cloud structure (Fig. 14a). This adds to the evidence implicating drizzle in the breakup of stratocumulus into open-cellular formations (Stevens et al. 2005; Petters et al. 2006; Sharon et al. 2006). Modeling studies by Feingold et al. (1996b) and Stevens et al. (1998) describe this link as an enhancement of updrafts in conditionally unstable regions below drizzling stratocumulus. Here, strong "cumulus-like" updrafts are instrumental in producing additional precipitation. The precipitation removes moisture from the parcel, and the drier air flows out from the core of the drizzle cell in the cloud layer and is associated with dry downdrafts that can break up the cloud layer. While high-resolution models have been able to capture cumuliform structures associated with drizzle, limitations in computational power have precluded simulations of the 20–30-km scales involved.

TABLE 3. Number of drizzle cells and columns in drizzle cells with reflectivity greater than or equal to 5 and 10 dB*Z* in each cloud-structure category. Table 1 lists the length of the data source in each category.

Category	Drizzle cells	Cores ≥5 dB*Z*	Cores ≥10 dB*Z*
Closed	293	53	14
Open	366	490	246
Unclassifiable	513	247	92

Recent observational studies have shown that aerosol concentrations are lower and drizzle rates are higher in "pockets of open cells" (Stevens et al. 2005; Kollias et al. 2004; Petters et al. 2006; Sharon et al. 2006). Lower aerosol concentrations are associated with fewer cloud condensation nuclei (CCN) and larger cloud drops per unit liquid water path, but can affect cloud properties and precipitation formation in either a posi-

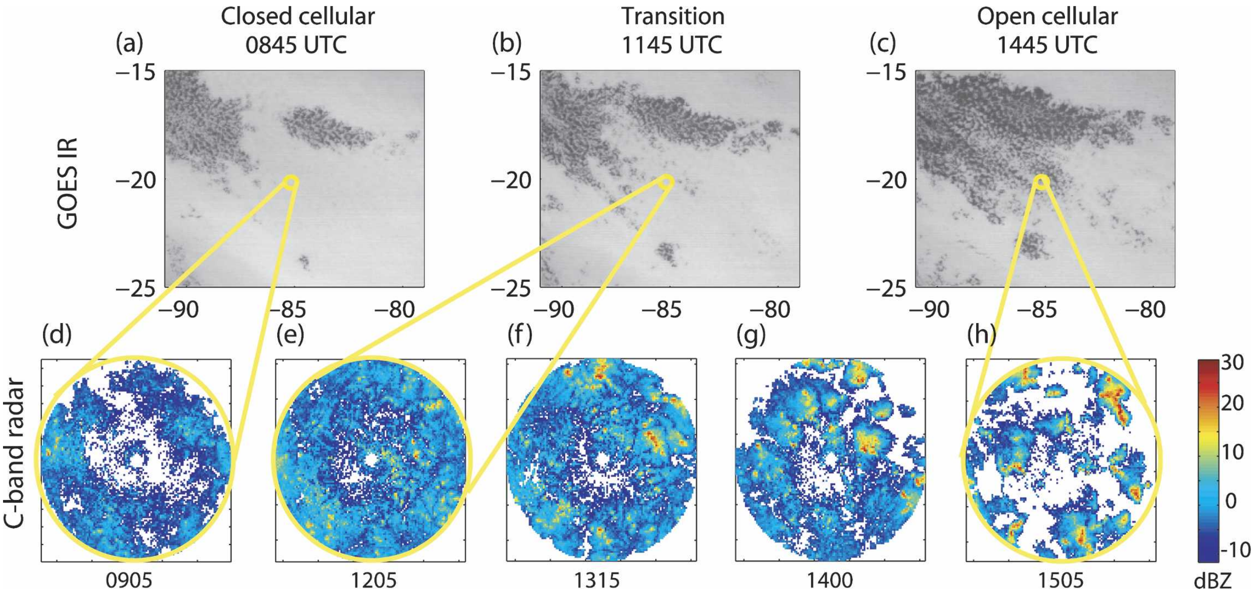

FIG. 13. Example of evolution from closed- to open-cellular cloud and drizzle structure. (a)–(c) GOES IR images at 0845, 1145, and 1445 UTC (0245, 0545, and 0845 LT, respectively) on 18 Oct 2001, plotted on a latitude–longitude grid. The images are classified as closed-cellular, unclassifiable, and open-cellular cloud structures, respectively. The satellite data are obtained at the ship position about 20 min later than the labeled image time. The ship positions at the time of the satellite overpass are marked in each image with yellow 30-km-radius circles. These correspond to 2D reflectivity maps from the C-band radar shown in (d)–(h). Reflectivity maps are also shown for 1315 and 1400 UTC corresponding to the transition in drizzle cell structure.

tive or negative sense (Albrecht 1989; Ackerman et al. 2004; Wood 2007). The high rain rates that accompany a transition from a closed- to an open-cellular cloud structure may be more likely to occur where there is a lower concentration of CCN. However, increased drizzle production reduces CCN concentration by scavenging aerosols (Feingold et al. 1996a; Wood 2006). Unfortunately, no in situ aerosol observations are available for this dataset. To untangle the web of cause and effect, future studies will need to carefully observe and

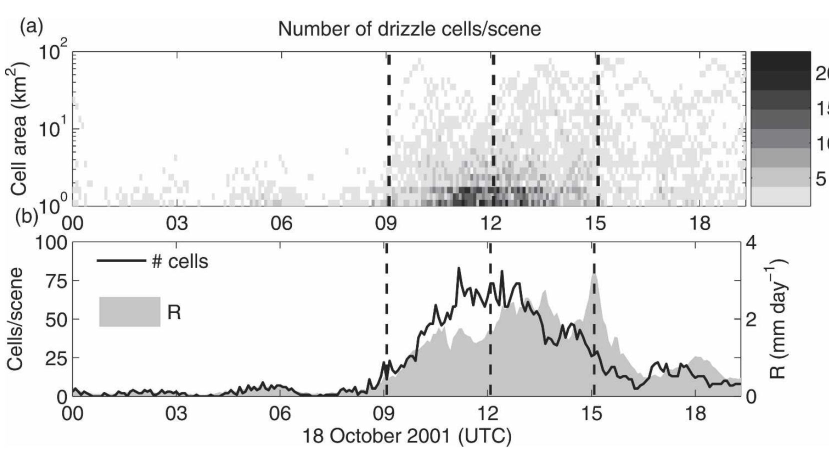

FIG. 14. Time series of (a) the number of drizzle cells in each evenly log-spaced area bin and (b) the total number of cells in each radar scene (solid) and area-averaged rain rate (shaded) corresponding to the transition example in Fig. 13. Satellite image times for Figs. 13a–c are marked with vertical dashed lines. Prior to the first satellite image time, the stratocumulus have a closed-cellular cloud structure, and at the time of the third image, the stratocumulus are open cellular. After the third image, the cloud structure continues to be open cellular for the duration of the period shown.

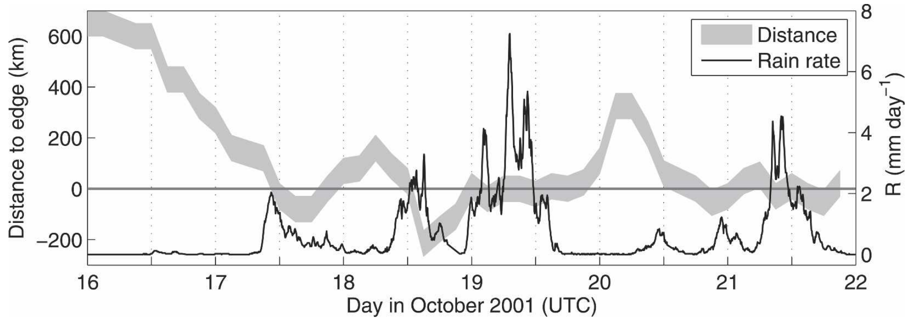

FIG. 15. Time series of straight-line distance between the ship and the nearest edge of an open-cellular region estimated from GOES IR images (gray shading shows approximate error in distance estimation) and area-averaged rain rates from the C-band radar (solid line). Positive distance indicates that the ship was in the closed-cellular region and negative distance indicates that the ship was in the open-cellular region. Vertical dotted lines indicate 0000 UTC (1800 LT) and 1200 UTC (0600 LT).

model cloud droplet and aerosol distributions and the evolution across the transition between closed- and open-cellular regions.

6. Conclusions

A unique set of joint satellite and scanning shipborne Doppler radar data observations of drizzling stratocumulus in the southeast Pacific during the EPIC Sc field campaign were examined. The observational period was divided into three categories based on visual inspection of infrared satellite images: closed-cellular and open-cellular cloud structure, and an unclassifiable category (Fig. 1). The latter included broken clouds that were not clearly or solely open cellular.

The larger sample size from the shipborne radar and the ability to examine both horizontal and vertical cross sections of drizzle cells over time has revealed important features of stratocumulus drizzle that were not discernible from the aircraft data used in previous studies. An important finding of this study is that radar-observed distributions of drizzle cell size and intensity are similar among the satellite cloud-structure categories, though in all cases the open-cellular distributions are shifted toward higher values. The distributions of rain-rate intensity and drizzle cell characteristics associated with different cloud structures (Fig. 2) represent a set of important characteristics that large eddy simulation (LES) models should be able to reproduce.

Both closed- and open-cellular regions exhibit a wide range of rain rates and reflectivity values. Smaller, weaker cells occur in drizzling scenes from all cloud-structure categories. Closed-cellular regions have lower area-average rain rates than open-cellular regions. The mode of the distribution of rain rates is shifted toward higher values within regions of broken clouds (open-cellular and unclassifiable scenes). Stronger and larger drizzle cells also occur preferentially in broken clouds (open-cellular and unclassifiable categories). These characteristics of drizzle cells among the cloud-structure types are consistent with other recent studies including Stevens et al. (2005, which was partly based on data from EPIC Sc), van Zanten and Stevens (2005), and Sharon et al. (2006).

While satellite observations of cloud structure may be useful to indicate the most likely distribution of rain rates associated with a set of scenes, identification of cloud structure alone does not provide sufficient information to use as a basis for developing routine precipitation retrievals. The observed distributions of rain-rate intensity do not yield distinct one-to-one relationships between specific rain rates and cloud-structure categories (Fig. 2). There is also low correlation between rain rate and cloud variability in terms of IR brightness temperature statistics (Figs. 3 and 4).

Boundary layer environmental conditions differ among closed-cellular, open-cellular, and unclassifiable cloud structures. Closed-cellular regions exhibit a well-mixed boundary layer and open-cellular regions have a less well mixed boundary layer (Table 3, Fig. 5). However, despite the differences in boundary layer environment, the ensemble kinematic and microphysical characteristics of drizzle cells are similar within regions with different cloud structures. Drizzle cells consist of contiguous regions with reflectivity ≥5 dBZ, as defined in section 3a. The ensemble statistics over all of the drizzle cells indicated precipitation growth within the cloud layer and evaporation beneath (Fig. 11), which is consistent with the analysis of drizzle cells in other stratocumulus regions (Vali et al. 1998; Wood 2005). Individual drizzle cells usually showed divergence near echo top and convergence below cloud base (Figs. 7–9). These patterns were observed on horizontal scales of roughly 2–20 km. Beneath a few strong drizzle cells, we found evidence of near-surface divergence marking cold pools created by evaporatively cooled downdrafts (Fig. 10). The overall drizzle cell structure is consistent with previous findings that evaporated moisture is recycled back into the cloud layer (Paluch and Lenschow 1991; Austin et al. 1995) and with recent conceptual models of drizzling stratocumulus (Comstock et al. 2005; van Zanten and Stevens 2005).

The combination of satellite and shipborne observations has revealed new insights into the transition from closed- to open-cellular cloud structure as well as the importance of the transition areas themselves to the regional dynamics. In the example presented in Figs. 13 and 14, the cloud structure over the ship transitioned from closed cellular through unclassifiable to open cellular. In this example, we saw that pockets of open cells can grow against the prevailing wind direction (Fig. 13). Large-scale flow divergence would expand the pockets of open cells only downstream, so this cannot be the sole mechanism to increase the area of these regions. During the transition, there was prolific development of radar-observed small drizzle cells (<10 km^2) that exceeded by over five times the number of total cells in either the preceding closed-cellular or following open-cellular periods (Fig. 14). As the cloud field evolved toward an open-cellular structure, larger cells developed (area >10 km^2) that were not present in the closed-cellular region. Peak area-average drizzle rate lagged by a few hours the peak in the total number of drizzle cells (Fig. 14). Based on evidence from EPIC Sc, the highest stratocumulus rain rates preferentially occur in open-cellular regions near the boundary or transition between closed- and open-cellular cloud structures.

The joint relationships between marine stratocumulus cloud structure and rain rate are strongly influenced by the diurnal cycle. When high area-average rain rates (>0.1 mm day^{-1}) appeared during EPIC Sc, they occurred in the early hours of the morning and within regions of higher cloud variability associated with broken clouds (open-cellular or unclassifiable cloud structures; Figs. 4 and 8). A larger sample of radar data is needed to determine fully representative probability distribution functions (PDFs) as a function of the diurnal cycle that can be used to estimate probabilities of rain rates associated with a particular cloud structure.

Observationally derived statistics such as those presented in this paper can be beneficial in evaluating model representations of stratocumulus properties. Future field programs such as the Variability of the American Monsoon Systems (VAMOS) Ocean–Cloud–Atmosphere–Land Study-Regional Experiment (VOCALS-Rex) will obtain airborne and shipborne radar measurements in the context of aerosol observations, the latter not available during EPIC Sc. Combining these observations will facilitate the exploration of the evolving microphysics and dynamics and the roles of aerosols and precipitation within open- and closed-cellular stratocumulus.

Acknowledgments. The authors express gratitude to the following people for their contributions to the data collection, analysis, and distillation: Peter Blossey, Sungsu Park, Wes Adkins, Robert Schaaf, Graham Feingold, Chris Fairall, Taniel Uttal, and the crew of the *RHB*. Bjorn Stevens and two anonymous reviewers also provided useful feedback. This research was funded by NSF ATM 0433712 and NASA PMM NNG04GA65G.

REFERENCES

Ackerman, A. S., M. P. Kirkpatrick, D. E. Stevens, and O. B. Toon, 2004: The impact of humidity above stratiform clouds on indirect aerosol climate forcing. *Nature,* **432,** 1014–1017.

Albrecht, B. A., 1989: Aerosols, cloud microphysics, and fractional cloudiness. *Science,* **245,** 1227–1230.

Atkinson, B. W., and J. W. Zhang, 1996: Mesoscale shallow convection in the atmosphere. *Rev. Geophys.,* **34,** 403–431.

Austin, P., Y. Wang, R. Pincus, and V. Kujala, 1995: Precipitation in stratocumulus clouds: Observations and modeling results. *J. Atmos. Sci.,* **52,** 2329–2352.

Bony, S., and J.-L. Dufresne, 2005: Marine boundary layer clouds at the heart of tropical cloud feedback uncertainties in climate models. *Geophys. Res. Lett.,* **32,** L20806, doi:10.1029/2005GL023851.

——, and Coauthors, 2006: How well do we understand and evaluate climate change feedback processes? *J. Climate,* **19,** 3445–3482.

Bretherton, C. S., T. Uttal, C. W. Fairall, S. E. Yuter, R. A. Weller, D. Baumgardner, K. Comstock, and R. Wood, 2004: The EPIC 2001 stratocumulus study. *Bull. Amer. Meteor. Soc.,* **85,** 967–977.

Comstock, K. K., 2006: Mesoscale variability and drizzle in southeast Pacific stratocumulus. Ph.D. thesis, University of Washington, 132 pp.

——, R. Wood, S. E. Yuter, and C. S. Bretherton, 2004: The relationship between reflectivity and rain rate in and below drizzling stratocumulus. *Quart. J. Roy. Meteor. Soc.,* **130,** 2891–2918.

——, C. S. Bretherton, and S. E. Yuter, 2005: Mesoscale variability and drizzle in southeast Pacific stratocumulus. *J. Atmos. Sci.,* **62,** 3792–3807.

Cronin, M. F., N. A. Bond, C. W. Fairall, and R. A. Weller, 2006: Surface cloud forcing in the East Pacific stratus deck/cold tongue/ITCZ complex. *J. Climate,* **19,** 392–409.

Feingold, G., S. M. Kreidenweis, B. Stevens, and W. R. Cotton, 1996a: Numerical simulations of stratocumulus processing of cloud condensation nuclei through collision-coalescence. *J. Geophys. Res.,* **101,** 21 391–21 402.

——, B. Stevens, W. R. Cotton, and A. S. Frisch, 1996b: The relationship between drop in-cloud residence time and drizzle production in numerically simulated stratocumulus clouds. *J. Atmos. Sci.,* **53,** 1108–1122.

Hartmann, D. L., M. E. Ockert-Bell, and M. L. Michelson, 1992: The effect of cloud type on Earth's energy balance: Global analysis. *J. Climate,* **5,** 1281–1304.

Houze, R. A., B. F. Smull, and P. Dodge, 1990: Mesoscale organization of springtime rainstorms in Oklahoma. *Mon. Wea. Rev.,* **118,** 614–654.

Jensen, J. B., S. Lee, P. B. Krummel, J. Katzfey, and D. Gogoasa, 2000: Precipitation in marine cumulus and stratocumulus. Part I: Thermodynamic and dynamic observations of closed cell circulations and cumulus bands. *Atmos. Res.,* **54,** 117–155.

Kingsmill, D. E., and R. M. Wakimoto, 1991: Kinematic, dynamic and thermodynamic analysis of a weakly sheared severe thunderstorm over northern Alabama. *Mon. Wea. Rev.,* **119,** 262–297.

Kollias, P., C. W. Fairall, P. Zuidema, J. Tomlinson, and G. A. Wick, 2004: Observations of marine stratocumulus in SE Pacific during the PACS 2003 cruise. *Geophys. Res. Lett.,* **31,** L22110, doi:10.1029/2004GL020751.

Krueger, A. F., and S. Fritz, 1961: Cellular cloud patterns revealed by TIROS I. *Tellus,* **13,** 1–7.

Leon, D. C., 2006: Observations of drizzle-cells in marine statucumulus. Ph.D. thesis, University of Wyoming. [Available from University Microfilm, 305 N. Zeeb Rd., Ann Arbor, MI 48106.]

Matejka, T. J., and R. C. Srivastava, 1991: An improved version of the extended velocity-azimuth display analysis of single-Doppler radar data. *J. Atmos. Oceanic Technol.,* **8,** 453–466.

Menzel, W. P., and J. F. W. Purdom, 1994: Introducing GOES-I: The first in a new generation of geostationary operational satellites. *Bull. Amer. Meteor. Soc.,* **75,** 757–780.

Minnis, P., P. W. Heck, D. F. Young, C. W. Fairall, and J. B. Snider, 1992: Stratocumulus cloud properties derived from simultaneous satellite and island-based instrumentation during FIRE. *J. Appl. Meteor.,* **31,** 317–339.

Moran, K. P., B. E. Martner, M. J. Post, R. A. Kropfli, D. C. Welsh, and K. B. Widener, 1998: An unattended cloud-profiling radar for use in climate research. *Bull. Amer. Meteor. Soc.,* **79,** 443–455.

Nicholls, S., 1984: The dynamics of stratocumulus: Aircraft observations and comparisons with a mixed layer model. *Quart. J. Roy. Meteor. Soc.,* **110,** 783–820.

Paluch, I. R., and D. H. Lenschow, 1991: Stratiform cloud formation in the marine boundary layer. *J. Atmos. Sci.,* **48,** 2141–2158.

Petters, M. D., J. R. Snider, B. Stevens, G. Vali, I. Faloona, and L. M. Russell, 2006: Accumulation mode aerosol, pockets of open cells, and particle nucleation in the remote subtropical Pacific marine boundary layer. *J. Geophys. Res.,* **111,** D02206, doi:10.1029/2004JD005694.

Rozendaal, M. A., C. B. Leovy, and S. A. Klein, 1995: An observational study of the diurnal cycle of marine stratiform cloud. *J. Climate,* **8,** 1795–1809.

Ryan, M., M. J. Post, B. Martner, J. Novak, and L. Davis, 2002: The NOAA *Ron Brown*'s shipboard Doppler precipitation radar. Preprints, *Sixth Symp. on Integrated Observing Systems,* Orlando, FL, Amer. Meteor. Soc., P1.7.

Sharon, T. M., B. A. Albrecht, H. H. Jonsson, P. Minnis, M. M. Khaiyer, T. M. van Reken, J. Seinfeld, and R. Flagan, 2006: Aerosol and cloud microphysical characteristics of rifts and gradients in maritime stratocumulus clouds. *J. Atmos. Sci.,* **63,** 983–997.

Stevens, B., W. R. Cotton, G. Feingold, and C.-H. Moeng, 1998: Large-eddy simulations of strongly precipitating, shallow, stratocumulus-topped boundary layers. *J. Atmos. Sci.,* **55,** 3616–3638.

——, and Coauthors, 2003: Dynamics and Chemistry of Marine Stratocumulus—DYCOMS II. *Bull. Amer. Meteor. Soc.,* **84,** 579–593.

——, G. Vali, K. Comstock, R. Wood, M. C. van Zanten, P. H. Austin, C. S. Bretherton, and D. H. Lenschow, 2005: Pockets of open cells (POCs) and drizzle in marine stratocumulus. *Bull. Amer. Meteor. Soc.,* **86,** 51–57.

Turton, J. D., and S. Nicholls, 1987: A study of the diurnal variation of stratocumulus using a multiple mixed layer model. *Quart. J. Roy. Meteor. Soc.,* **113,** 969–1009.

Vali, G., R. D. Kelly, J. French, S. Haimov, R. E. M. D. Leon, and A. Pazmany, 1998: Finescale structure and microphysics of coastal stratus. *J. Atmos. Sci.,* **55,** 3540–3564.

van Zanten, M. C., and B. Stevens, 2005: On the observed structure of heavily precipitating marine stratocumulus. *J. Atmos. Sci.,* **62,** 4327–4342.

——, ——, G. Vali, and D. H. Lenschow, 2005: Observations of drizzle in nocturnal marine stratocumulus. *J. Atmos. Sci.,* **62,** 88–106.

Wood, R., 2005: Drizzle in stratiform boundary layer clouds. Part I: Vertical and horizontal structure. *J. Atmos. Sci.,* **62,** 3011–3033.

——, 2006: The rate of loss of cloud condensation nuclei by coalescence in warm clouds. *J. Geophys. Res.,* **111,** D21205, doi:10.1029/2006JD007553.

——, 2007: Cancellation of aerosol indirect effects in marine stratocumulus through cloud thinning. *J. Atmos. Sci.,* **64,** 2657–2669.

——, and D. Hartmann, 2006: Spatial variability of liquid water path in marine low cloud: The importance of mesoscale cellular convection. *J. Climate,* **19,** 1748–1764.

Wyant, M. C., C. S. Bretherton, J. T. Bacmeister, J. T. Kiehl, I. M. Held, M. Zhao, S. A. Klein, and B. J. Soden, 2006: A comparison of low-latitude cloud properties and their response to climate change in three AGCMs sorted into regimes using mid-tropospheric vertical velocity. *Climate Dyn.,* **27,** 261–279.

Yuter, S. E., and R. A. Houze, 1995: Three-dimensional kinematic and microphysical evolution of Florida cumulonimbus. Part II: Frequency distribution of vertical velocity, reflectivity, and differential reflectivity. *Mon. Wea. Rev.,* **123,** 1941–1963.

——, Y. L. Serra, and R. A. Houze, 2000: The 1997 Pan American Climate Studies Tropical Eastern Pacific Process Study. Part II: Stratocumulus region. *Bull. Amer. Meteor. Soc.,* **81,** 483–490.

——, R. A. Houze Jr., E. A. Smith, T. T. Wilheit, and E. Zipser, 2005: Physical characterization of tropical oceanic convection observed in KWAJEX. *J. Appl. Meteor.,* **44,** 385–415.